Characterization of FeSi2.9 and SS 316L Produced by Directed Energy Deposition for Bimetallic High-Speed Rotors

Proceedings of the ASME 2025 20th International Manufacturing Science and Engineering Conference
MSEC2025
June 23-27, 2025, Greenville, South Carolina

MSEC2025-155456

CHARACTERIZATION OF $FeSi_{2.9}$ AND SS 316L PRODUCED BY DIRECTED ENERGY DEPOSITION FOR BIMETALLIC HIGH-SPEED ROTORS

Chiara Gianassi
Department of Industrial Engineering, University of Bologna, Bologna, Italy

Erica Liverani
Department of Industrial Engineering, University of Bologna, Bologna, Italy

Alessandro Ascari
Department of Industrial Engineering, University of Bologna, Bologna, Italy

Andrea Tonoli
Department of Mechanical and Aerospace Engineering, Polytechnic of Turin, Turin, Italy

Andrea Cavagnino
Department of Energy, Polytechnic of Turin, Turin, Italy

Alessandro Fortunato
Department of Industrial Engineering, University of Bologna, Bologna, Italy

ABSTRACT

The high-speed electric machinery sector has experienced significant growth over the last decade. Permanent magnet motors dominate this sector thanks to their superior torque volumetric density and efficiency compared to other AC magnet-free electrical machines, but their reliance on rare earth elements raises cost, supply chain issues, and environmental concerns. To address this, Synchronous Reluctance (SynRel) motors, which do not employ permanent magnets, are being explored. However, their mechanical limitations restrict rotor speed when produced with the internal flux barriers cuts. Additive manufacturing (AM), particularly Directed Energy Deposition (DED), enables the production of multi-material structures, allowing to overcome these limitations.

For high-speed rotors, FeSi alloys are excellent soft magnetic materials, thanks to their high magnetic permeability. AISI 316L austenitic stainless steel has a magnetic permeability similar to that of air; therefore, it can substitute the structural cuts and act as a flux barrier while providing mechanical strength. Although both materials have been studied in AM processes, no comprehensive research has focused on DED's potential for multi-material printing. This work aims to fill that gap by assessing DED's ability to produce high quality $FeSi_{2.9}$ and 316L structures for bimetallic electric rotors.

The experimental campaign involved the fabrication of specimens for microstructural, mechanical and magnetic characterization, starting from gas-atomized powders. Both materials were characterized in terms of particle size distribution and chemical composition prior to printing. The printed specimens underwent the same annealing process (850°C for 1 hour, followed by air cooling). Although the treatment aimed to improve the magnetic properties of FeSi, it was also applied to the 316L stainless steel to evaluate its effect, with a view toward subsequent bimetallic printing. The microstructures were examined before and after heat treatment through optical and scanning electron microscopy, focusing on chemical composition, grain size and morphology. Vickers microhardness tests were performed on both as-printed and annealed samples, showing a consistent trend along the deposition height for all specimens. Additionally, magnetic tests were conducted on toroidal samples to evaluate the BH curves and specific loss trends at different excitation frequencies. Finally, tensile tests were used to measure the mechanical properties of both materials, highlighting the ductility of 316L and the brittle behavior of the $FeSi_{2.9}$.

The results indicated that both materials exhibited excellent printability, achieving crack-free depositions with relative densities greater than 99%. The combination of $FeSi_{2.9}$ and AISI 316L offers promising prospects for developing DED-printed synchronous reluctance rotors with enhanced performance and operational speed capabilities.

Keywords: Laser Processes, Powder Processing, Direct Energy Deposition, Soft Magnetic Materials, Stainless Steel, Bimetallic Additive Manufacturing, High Speed SynRel Motors.

1. INTRODUCTION

The high-speed electric machinery sector has experienced significant growth over the past decade. In high-speed applications, permanent magnets (PM) motors play a crucial role due to their high efficiency and capability to operate over a wide range of speeds [1]. The main alloys used in the manufacture of permanent magnets are NdFeB, thanks to its cost-performance balance, and SmCo, which guarantees thermal stability at high temperatures [2]. However, the reliance on rare earth elements (REEs) in permanent magnets makes them subject to significant price fluctuations; additionally, the extraction and processing of REEs raises serious social and environmental concerns. In response, the European Union is actively funding research efforts aimed at developing solutions that avoid the use of rare earth materials. Among these, many studies have focused on investigating the potential of Synchronous Reluctance (SynRel) motor technology for high-speed applications that do not require permanent magnets. The primary challenge lies in the mechanical weakness of their rotor structures, which normally limits their use to speeds below 20-30 krpm [3]. SynRel motors, indeed, have cuts in the cylindrical structure designed to introduce internal flux barriers. However, these cuts compromise the mechanical stiffness of the rotor, limiting its operational speed. To address this drawback, metal additive manufacturing (AM) techniques enable the production of more complex designs and offer the possibility of producing multi-material structures. Newman et al. [4] utilized Laser Powder Bed Fusion technology to produce bi-material tensile specimens and toroids, composed of half $FeSi_{3.5}$ and half 316L stainless steel. Their study aimed to characterize these materials for the development of a multi-material electric rotor. Additionally, they optimized the design of a four-pole rotor capable of reaching 55 krpm, demonstrating that additively manufactured rotors can overcome the speed limitations of conventionally manufactured counterparts. However, the traditional architecture of LPBF systems does not allow for multi-material printing, as a complex material change procedure would be required at every layer. Among all metal additive manufacturing technologies, Directed Energy Deposition (DED) processes are particularly promising due to their versatility. A comprehensive review of the multi-material applications of DED processes was conducted by Feenstra et al. [5], highlighting how these technologies enable the fabrication of bimetallic, functionally graded, and hybrid components. Among hybrid strategies, the production of layered materials presents a significant challenge of great interest, despite the difficulties associated with the low resolution of DED processes. For instance, Chen et al. [6] created structures composed of alternating layers of 316L and Inconel 625, studying the phenomena occurring at the interface between the two materials from a thermodynamic and microstructural perspective. Based on these studies, DED technology enables the production of components with alternating layers of different materials, with much simpler powder handling compared to LPBF technologies. This approach can be applied to the manufacturing of a high-speed synchronous reluctance rotor. The flux barriers can be replaced with layers of paramagnetic material, allowing for increased mechanical stiffness, thus expanding the operational speed range [7]. Moreover, eliminating the parasitic magnetic bridges enhances the saliency of the machine. For such high-speed applications (e.g., 100 krpm), these gaps would need to be significantly thick, which would severely affect both the magnetic properties and the mechanical stiffness of the rotor. The limitation related to the low dimensional accuracy can be overcome by subjecting the workpiece to subsequent machining operations. The choice of materials must be based on their specific properties and their chemical compatibility. For magnetic materials high permeability, high saturation, high electrical resistivity, and high thermal conductivity are required [8]. However, the material must also be compatible with DED technologies. Iron-silicon alloys are among the most suitable soft magnetic materials for this application. Studies on both LPBF [9] and DED [10] technologies have shown that pure iron exhibits excellent printability, achieving relative densities up to 99.7%. The addition of silicon helps reduce eddy current losses, but it also negatively affects the alloy's processability in laser additive manufacturing. Garibaldi et al. [11] demonstrated that $FeSi_{6.9}$ shows a higher tendency to form cracks and microstructural defects. A silicon content around 2.5-3.5% in weight appears to offer a good compromise between printability and magnetic properties in both LPBF [4] and DED technologies [12], [13]. As for the flux barrier material, the primary requirements are a magnetic permeability similar to that of air and mechanical properties comparable to those of the ferromagnetic material. Austenitic stainless steel 316L meets these criteria and is frequently used with Directed Energy Deposition technologies thanks to its excellent printability [14], [15]. Although there are studies in the literature on the printing of these materials, especially using LPBF technology, there are no cases where these materials have been deposited using DED technology and characterized from the perspective of bi-material printing. In this experiment, the DED process was used to print $FeSi_{2.9}$ and AISI 316L austenitic stainless steel. The materials underwent heat treatment and were characterized mechanically through tensile tests and microhardness measurements, as well as magnetically. Additionally, the microstructure of both materials was analyzed before and after annealing using optical and electron microscopy, with the aim of assessing the effect of the treatment on grain shape and size. This characterization was carried out with a view to a future multi-material application, specifically for the fabrication of a synchronous reluctance rotor composed of alternating layers of magnetic and paramagnetic materials. Therefore, a preliminary assessment of chemical compatibility was conducted by printing alternating layers of the two materials, verifying the absence of inter and intra-layers defects.

2. MATERIALS AND METHODS

2.1 Specimen fabrication and heat treatment

The experimental campaign focused on the printing of two distinct metal alloys – one ferromagnetic and one paramagnetic – aimed at characterizing them before subsequent multi-material printing. $FeSi_{2.9}$ (Figure 1a) supplied by m4p Material Solutions GmbH (Austria), with 2.9 wt% of Si, was selected as the soft magnetic material, with powder particle sizes ranging from 45 to 106 μm. The paramagnetic material chosen for the study was austenitic stainless steel AISI 316L (Figure 1b) supplied by

Heeger Materials Inc. (CO, US) with a particle size range of 53-150 µm.

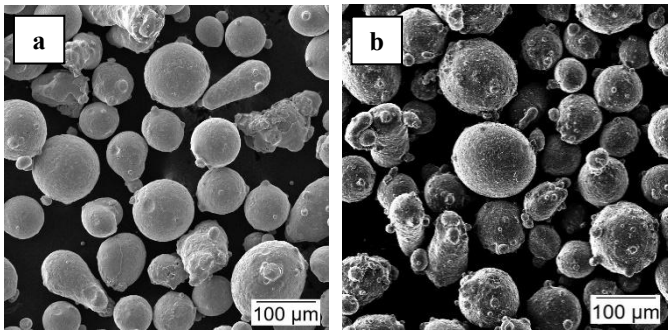

FIGURE 1: FESEM IMAGES OF $FeSi_{2.9}$ (a) AND AISI 316L (b) POWDER PARTICLES

For both materials, the powder samples were examined in their as-received condition. Particle size distribution and chemical composition were assessed using a scanning electron microscope (Tescan Mira3 with a Schottky Emitter) coupled with an EDS system (Bruker X-Flash 630M) for micro-elemental analysis, and subsequently quantified through image analysis with the open-source software ImageJ. Tables 1 and 2 report the results obtained from particle characterization, while Figure 2 reports the particle size distribution of both materials.

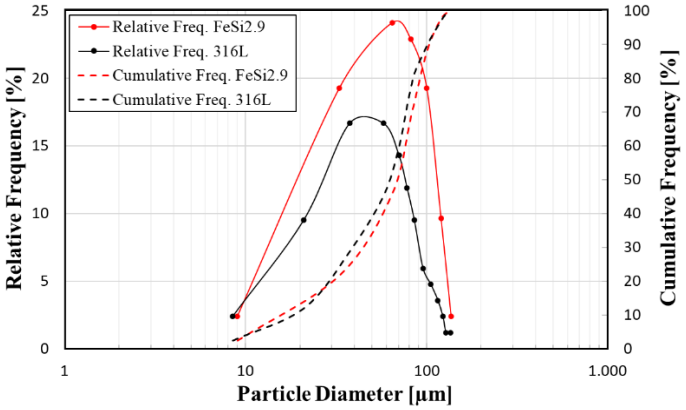

FIGURE 2: PARTICLE SIZE DISTRIBUTION OF 316L AND FeSi2.9 POWDERS

TABLE 1: CHEMICAL COMPOSITION OF THE PARTICLES EVALUATED BY FESEM-EDS

[wt %]	Fe	Si	Cr	Mn	Ni	Mo
AISI 316L	bal.	1.15	17.2	1.65	10.5	2.39
$FeSi_{2.9}$	bal.	3.36	-	-	-	-

TABLE 2: PARTICLE SIZE DISTRIBUTIONS

	D10 [µm]	D50 [µm]	D90 [µm]
AISI 316L	18. 6	64.7	121.2
$FeSi_{2.9}$	16.2	70.7	111.0

Deposition tests were conducted on a Fe substrate (> 99.95% purity) with a thickness of 15 mm. The selection of an extra-soft steel as the base material was made to ensure a minimal carbon content, thus preventing surface hardening when exposed to the concentrated thermal energy delivered by the laser beam.

Specimens were manufactured using a Direct Energy Deposition system that integrates a 6-axis ABB IRB 4600 robot and a 2-axis IRBP A250 roto-tilting positioner. The system is equipped with a Laserline LDF-4500-60 diode laser capable of delivering a maximum power of 4.5 kW, coupled with a feeding fiber with a core diameter of 600 µm. The laser features Laserline OTS-5 focusing optics with a collimating focal length of 80 mm and a 300 mm focusing length, resulting in a 2.2 mm spot diameter on the surface. Powder delivery is handled by a GTV PS2/2 feeder system and a GTV PN6625 six-outlets nozzle, maintaining a standoff distance of 25 mm and a powder jet focus of 2 mm. Argon was selected as the carrier and shielding gas, with flow rates of 8 l/min and 20 l/min, respectively.

To evaluate the properties of the individual materials, various samples were produced. Specifically, a 30x40 mm specimen consisting of six layers was deposited for both materials. Additionally, four parallelepiped blanks (two from $FeSi_{2.9}$ and two from AISI 316L), each measuring 30x90x10 mm, were printed to later extract tensile specimens. The Roboris Eureka software was finally used to generate the slicing strategy for fabricating toroids, from which samples for magnetic characterization were obtained. In total, two rings with an internal diameter of 65 mm, an external diameter of 85 mm and a height of 15 mm were printed for each material. For clarity, the list of single-material deposited geometries has been outlined in Table 3 and the geometries are depicted in Figure 3. Moreover, in order to evaluate the compatibility between the two materials, a 30x40x10 bimetallic specimen was fabricated, consisting of alternating groups of two layers of $FeSi_{2.9}$ and AISI 316L. The scanning strategy for the parallelepipeds, microstructural samples and bimetallic specimen involved first the deposition of the contour, followed by a back-and-forth fill pattern with a 50% overlap between tracks. Each successive layer was rotated 90° relative to the previous one, altering the starting point of deposition and the filling direction. The toroid blanks were fabricated by adopting a concentric scanning strategy, with a random starting point for each layer to prevent material buildup.

The process parameters detailed in Table 4 were used to produce both the single-material geometries and the bimetallic specimen. The laser power was gradually decreased with the increasing of deposited layers, preventing excessive energy concentration. In Table 4, the first value represents the initial power (maximum value), the second indicates the final power (minimum value), and the third indicates the power reduction applied after each layer. The table also reports the specific energy values (E), calculated as:

$$E = \frac{P}{v \cdot D} \quad (1)$$

where P is the laser power, v is the scan velocity, and D is the laser spot diameter. For the calculation, the initial power was considered. The process parameters for AISI 316L were optimized in previous studies [14], and similar parameters were selected for printing $FeSi_{2.9}$. The resulting specific energy aligns with values reported by [10] and [13] for the printing of pure Fe and $FeSi_{2.5}$, respectively, with DED technology.

TABLE 3: LIST AND DESCRIPTION OF PRINTED GEOMETRIES FOR EACH MATERIAL

#	Description	Quantity	Scan Strategy	Geometry	Heat treated
1	Sample for OM-SEM analysis	1	Back and forth fill pattern	Parallelepiped 30x40 mm, 6 layers	½ yes, ½ no
2	Bulk for tensile specimens	2	Back and forth fill pattern	Parallelepiped 90x30xh10 mm	Yes
3	Bulk for magnetic tests	2	Concentric	Toroid, $D_{ext\text{-}int}$=85-65 mm, h=15 mm	Yes

TABLE 4: LIST OF PROCESS PARAMETERS EMPLOYED FOR THE PRINTNG OF COMPONENTS IN TABLE 3

	Scan velocity, v [mm·min^{-1}]	Laser power, P [W]	Powder flow rate, g [g·min^{-1}]	Layer height, Δz [mm]	Specific energy, E [J·mm^{-2}]
AISI 316L	1020	2200-2000-80	9.1	0.7	58.8
FeSi$_{2.9}$	1200	2000-1800-80	10	0.8	45.5

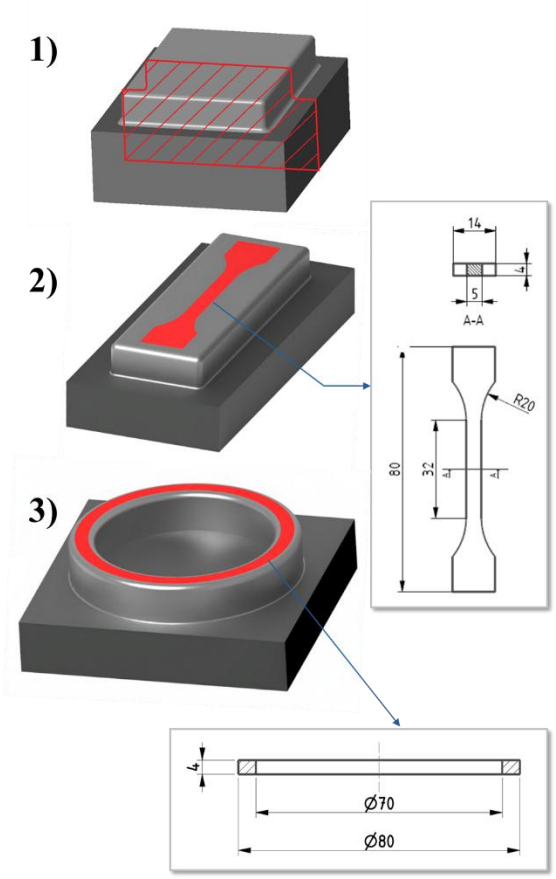

FIGURE 3: GEOMETRY OF THE DED-DEPOSITED BULKS

With a view to the multi-material application, the same heat treatment was applied to $FeSi_{2.9}$, AISI 316L and bimetallic samples, with the primary goal of enhancing the magnetic properties of $FeSi_{2.9}$. Garibaldi et al. [16] optimized the annealing process for $FeSi_{6.9}$ samples produced using Laser Powder Bed Fusion, testing temperatures from 400°C to 1150°C. Their study showed that the magnetic permeability increases with higher annealing temperatures, but the peak at 1150°C was linked to significant grain growth, potentially compromising mechanical properties. Lee et al. [12] also investigated annealing on $FeSi_{3.5}$ DED-samples. Their results demonstrate similar improvements in magnetic properties with increasing temperature, confirming that the findings of Garibaldi et al. are also valid for DED samples. Finally, Zanni et al. [9] applied an 850°C annealing treatment to LPBF samples of pure Fe, selecting a lower temperature to avoid the α-Fe to γ-Fe phase transition at 911°C. Regarding AISI 316L, Xiao et al. [15] found that annealing at 850°C on DED-produced samples effectively relieved stress. Based on these studies, an annealing treatment at 850°C for 1 hour with air cooling was selected for both $FeSi_{2.9}$ and AISI 316L. The samples for microstructural analysis were cut in two by using EDM: one half was analyzed in the as-built condition, while the other was subjected to heat treatment, along with the other bulks.

2.2 Microstructural analysis and hardness tests

For both AISI 316L and $FeSi_{2.9}$, including as-built and heat-treated samples, the following procedure was adopted for microstructural analysis: metallographic samples were prepared by cutting cross-sections from each deposition using wire electrical discharge machining (W-EDM). These sections were mounted and ground with progressively finer silicon carbide (SiC) sandpapers, followed by polishing with 1 µm alumina. Initial defect assessment was conducted using an optical microscope (Zeiss AXIO Observer A1m), and relative density was calculated with ImageJ software. To reveal the microstructure, chemical etching was performed with Nital for $FeSi_{2.9}$ and Vilella's reagent for AISI 316L for a swab time of 10 s and 45 s, respectively. The etched samples were subsequently examined using a high-resolution optical microscope (Keyence VHX-7000) and a scanning electron microscope (Tescan Mira3 with a Schottky emitter) with EDS probe. Finally, Vickers microhardness tests were performed on both the as-is and heat-treated samples using a Remet HX-1000 microdurometer. A load of 0.2 kg (HV0.2) was applied for a dwell time of 10-15 seconds, in accordance with ISO 6507-1:2023. For each specimen, seven measurements were taken along a vertical path in the middle of the deposition, following the growth direction, with indentations spaced 0.5 mm apart.

2.3 Magnetic and mechanical characterization

For the magnetic tests, two toroids were produced for each material, starting from the deposited oversized bulk already annealed. The toroids were machined by turning to achieve the final dimensions of 80 mm in outer diameter, 70 mm in inner diameter, and 4 mm in thickness (Figure 3). The ring-core

specimens were wound with a magnetizing coil consisting of 110 turns and a sensing coil with 40 turns. The samples were then tested according to EN IEC 60404-6:2018 standard using the ad-hoc test bench and data acquisition system developed by the authors and described in [17].

For the production of tensile specimens, two oversized rectangular blocks were printed for each material. The bulks underwent the same heat treatment as the toroids and other samples. Subsequently, the specimens were cut according to the geometry illustrated in Figure 3 using W-EDM. Quasi-static tensile tests were conducted in accordance with BS EN ISO 6892 using a hydraulic testing machine (Italsigma, Forlì, Italy) equipped with a 20 kN load cell. During the tests, the crosshead separation rate was maintained at a constant value of 0.17 $mm \cdot min^{-1}$, and strain was measured with an extensometer with a gauge length of 25 mm. An engineering stress-strain curve was obtained for each specimen, allowing the calculation of the 0.2% proof stress ($R_{p0.2}$), the ultimate tensile strength (UTS) and the elongation to fracture ($A_{\%}$). Finally, SEM images of the specimens' fracture surfaces were taken.

3. RESULTS

3.1 Microstructural analysis

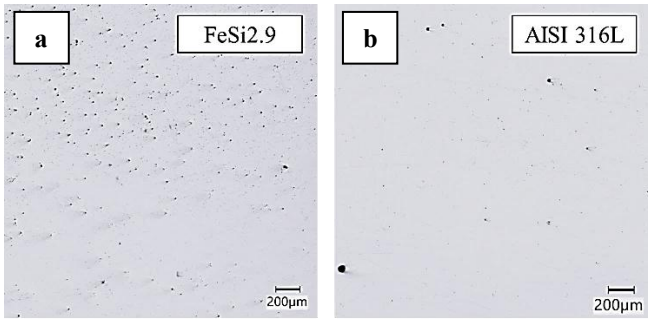

$\rho_{rel} = 99.4\%$ $\rho_{rel} = 99.7\%$

FIGURE 4: RELATIVE DENSITY OF $FeSi_{2.9}$ (a) AND 316L (b) AND OPTICAL MICROSCOPE IMAGES

Figure 4 presents optical microscope images of the sections used for calculating relative densities. Since the heat treatment does not affect porosity, only the images and percentages corresponding to as-built samples are reported. The density analysis primarily aims to verify that the selected process parameters do not result in significant microstructural defects. As shown in Figure 4a, the $FeSi_{2.9}$ sample exhibits porosity that is generally smaller in size but more widespread throughout the deposition. Nonetheless, it achieves a high relative density (99.4%), consistent with values obtained by [10] in DED printing of pure Fe. For the 316L stainless steel (Figure 4b), the porosity is, on average, larger in size but much less widespread, resulting in a density of 99.7%. Given the absence of cracks and the high observed density, it can be concluded that the process parameters selected are optimal for both alloys and suitable for subsequent prints.

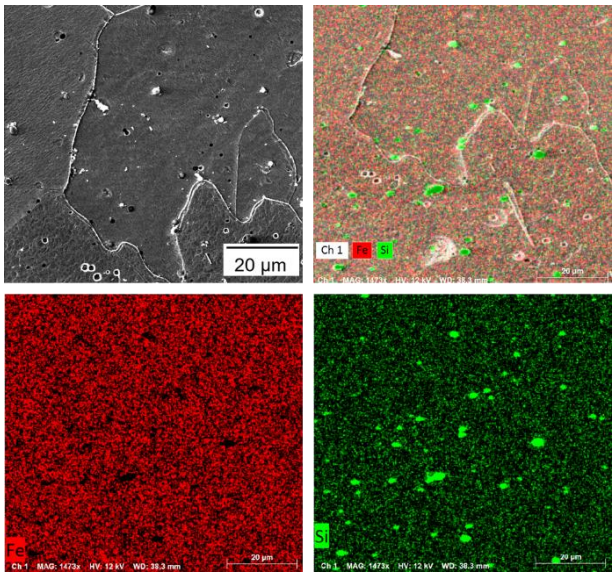

FIGURE 5: COMPOSITIONAL MAPS OF AS-IS $FeSi_{2.9}$

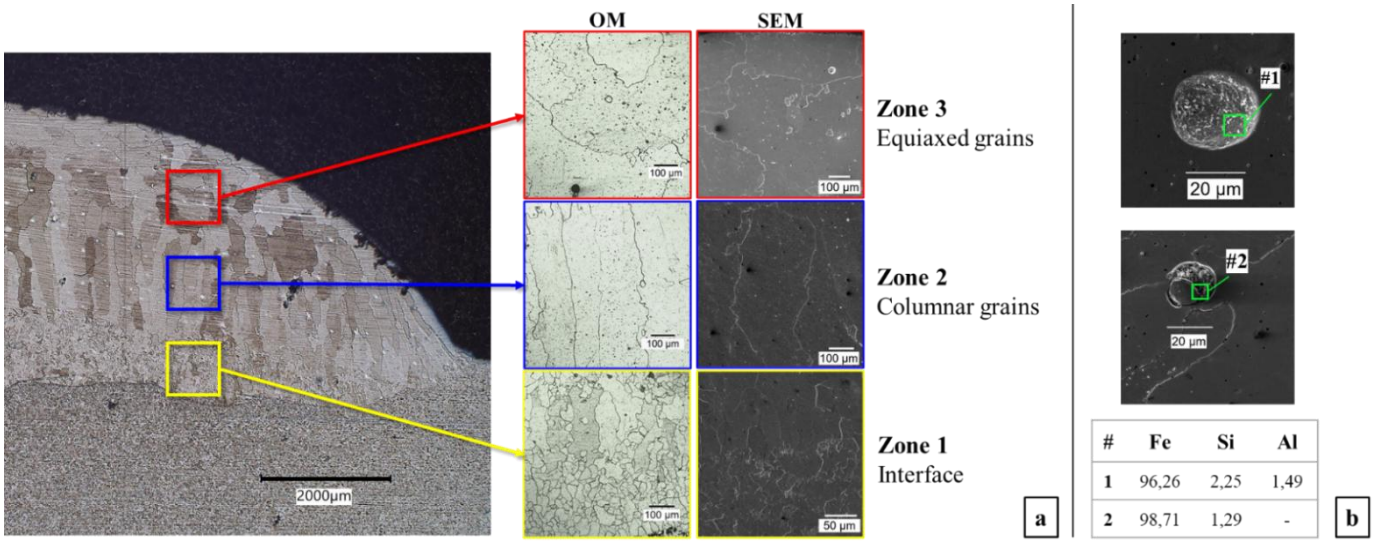

#	Fe	Si	Al
1	96,26	2,25	1,49
2	98,71	1,29	-

FIGURE 6: SEM AND OM IMAGES OF THE GRAIN MORPHOLOGY OF HEAT TREATED $FeSi_{2.9}$ (a); SEM IMAGES AND CHEMICAL COMPOSITIONS OF DEFECTS (b)

For microstructural characterization, results from optical and electron microscopy after etching were compared. Figure 5 displays the compositional map obtained using SEM with an EDS probe of a portion of the untreated $FeSi_{2.9}$ sample. The lack of distinguishable grain boundaries in the Fe and Si distribution maps indicates no differences between the boundaries and the grain interiors. Conversely, the presence of Si-rich particles suggests a segregation phenomenon. After heat treatment, these particles disappear, as shown in the SEM images in Figure 6a; this change could be attributed to the dissolution of silicon into the solid, as stated by [16]. The chemical etching performed on the $FeSi_{2.9}$ samples, both before and after treatment, reveals three regions with distinct microstructures (Figure 6a). At the interface, the grains tend to be smaller, with no preferential orientation. This is due to the rapid heat dissipation in the initial layers of the material, which prevents grain growth. In this region, the silicon content is limited to 2% for both samples due to dilution with the base material, which is composed entirely of Fe. As the distance from the interface increases, the grains take on a columnar shape and elongate parallel to the direction of heat flow and perpendicular to the interface [18]. The Si content also increases, reaching a maximum of 2.4%. Finally, in the upper part of the deposition, the grains lose their preferential orientation and grow larger, forming an equiaxed structure. The heat treatment does not alter the microstructure morphology, which remains divided into three distinct zones. However, a widespread increase in grain size is observed. Lee et al. [12] reported that annealing $FeSi_{3.5}$ at 900°C results in residual stress relief, along with grain enlargement. This positively affects magnetic properties, as grain boundaries act as defects that hinder demagnetization, and increasing the grain size reduces their concentration [16]. Figure 6b provides two high-magnification images of spherical defects in the treated sample. EDS analysis reveals that the composition is identical to the surrounding material, except for a small amount of Al, likely from polishing residue with alumina. The composition, along with the spherical shape and size, suggests that these are unmelted powder particles embedded within the solid matrix. Figure 7 displays the main results from microscopy analysis of both treated and untreated 316L stainless steel specimens. Since heat treatment did not produce significant effects on 316L, the evaluation of both samples was conducted without distinction. As shown in Figure 7a, chemical etching on SS 316L highlights the melt pools created by the laser passes. The 90° rotation of the laser path for each layer is evident in the micrograph, comparable to results obtained by Ribeiro et al. [19] with the same scanning strategy, where alternating tracks cut along the long and short sides are observed. Grain morphology is more visible in the SEM images (Figures 7c-7d). In the central region, a predominantly columnar structure is apparent, while at the top the grains tend to be equiaxed. This mixed microstructure was also observed by Zheng et al. [20], who reported alternating regions of equiaxed grains, fine columnar grains, and coarsened columnar grains. At higher magnifications, dendrites can be observed growing in a direction as close as possible to the isotherm. In DED-printed austenitic stainless steel, the predominant phase consists of austenite cells with intercellular ferrite [20]. Compositional analysis performed on an image of the dendrites (Figure 7e) reveals an enrichment of Cr and Mo in the intercellular region (white). The higher concentration of these elements in the intercellular zone is likely due to the advancing solidification front, which prevented them from fully dissolving into the dendritic structure.

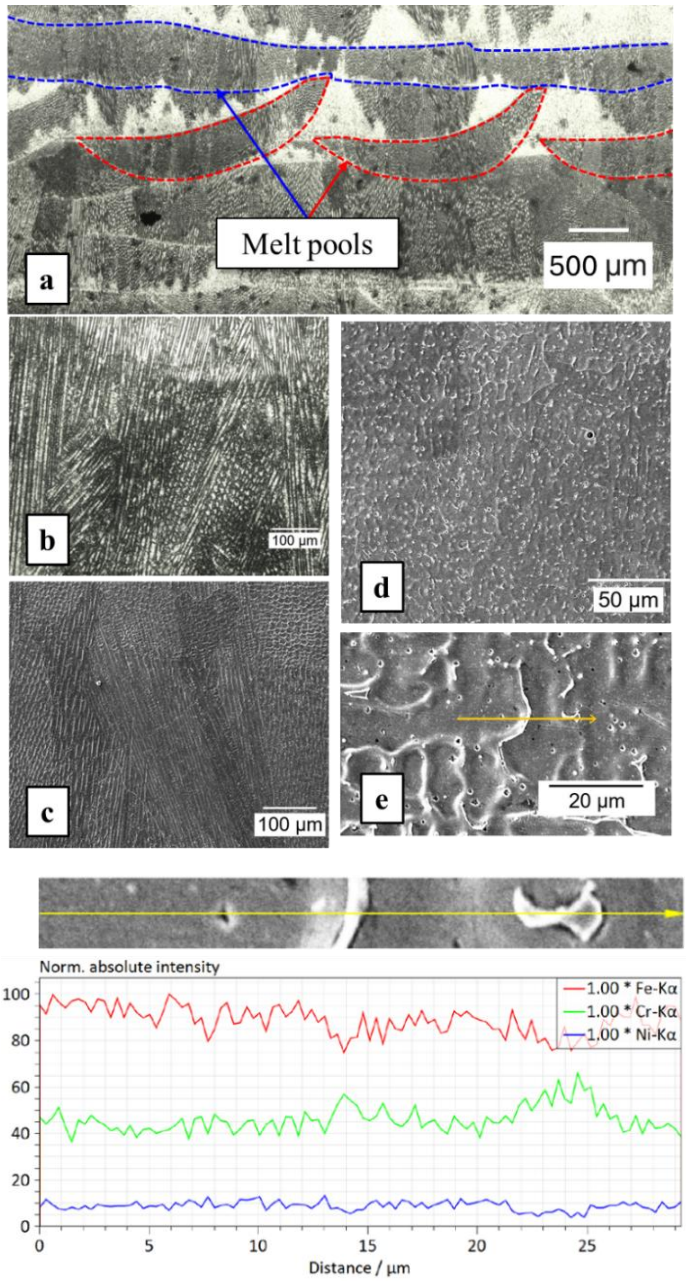

FIGURE 7: SEM AND OM IMAGES OF THE MELT POOLS (a) AND MICROSTRUCTURE (b-d) OF AISI 316L; EDS CHEMICAL COMPOSITION OF DENDRITES (e)

Finally, to verify the compatibility between the materials, the multi-material print test was analyzed. A cross-sectional analysis of the deposition, reported in Figure 8, demonstrates the absence of interfacial defects, such as cracks or delamination phenomena, allowing for further analysis. Given the absence of defects and the proper dilution between the layers, the interfacial adhesion results are promising.

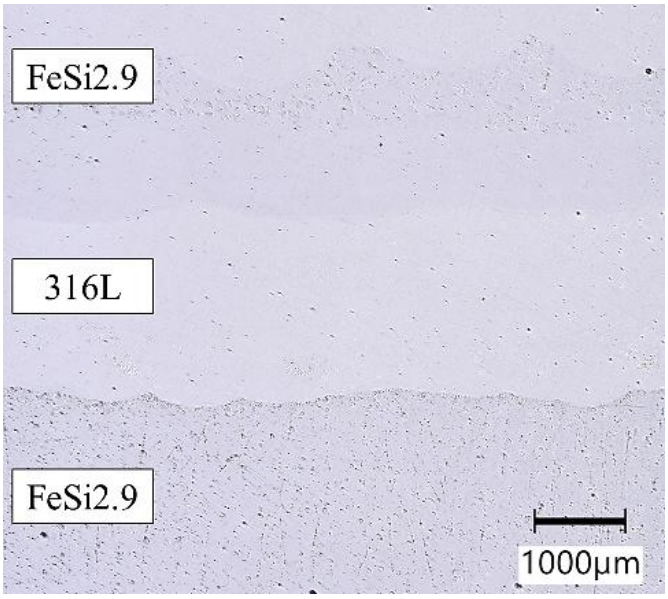

FIGURE 8: SECTION OF THE MULTI-MATERIAL PRINT

3.2 Microhardness tests

Figure 9 displays the results of the microhardness tests. Specifically, Figure 9a illustrates the trend as a function of the distance from the substrate for both treated (HT) and untreated (NT) materials, while Figure 9b shows the average microhardness values and their standard deviations for the four experimental cases. In both materials, the graphs show a fairly consistent trend along the deposition height, with standard deviations below 10 HV. This behavior suggests that the alloying elements are uniformly distributed within the deposition, as confirmed by SEM compositional analysis. Moreover, this trend persists even after heat treatment, indicating that the annealing process performed on the samples does not affect the macroscopic distribution of alloying elements. The AISI 316L sample in its as-built condition shows a microhardness of approximately 197 HV. This value aligns with the results obtained by [14], who conducted Rockwell hardness tests on AISI 316L samples fabricated with the same process parameters. Xiao et al. [15] also investigated the mechanical properties of a DED-printed AISI 316L component, evaluating the effect of the heat treatment. Their findings are fully consistent with those of our study, showing a microhardness of 208 HV in the as-built condition and 176 HV after annealing at 850°C for 2 hours. According to the authors, this reduction in hardness can be attributed to stress relief induced by heat treatment. Before heat treatment, the $FeSi_{2.9}$ sample exhibits an average microhardness of 205 HV. Although there are no studies in literature using the same material and technology, Lee et al. [12] conducted Vickers hardness tests on $FeSi_{3.5}$ samples fabricated via Directed Energy Deposition. Their study reports an average microhardness of 284 HV, which is higher than the value obtained in this study. This difference is likely due to the higher silicon content in their powders. After heat treatment, a 14.6% reduction in hardness was observed. Zanni et al. [9] applied the same heat treatment to pure iron specimens produced by Laser Powder Bed Fusion technology, and their results showed a hardness reduction comparable to the one found in the present work. According to them, this reduction can be explained by a decrease in dislocation density caused by annealing, which limits the strengthening effect.

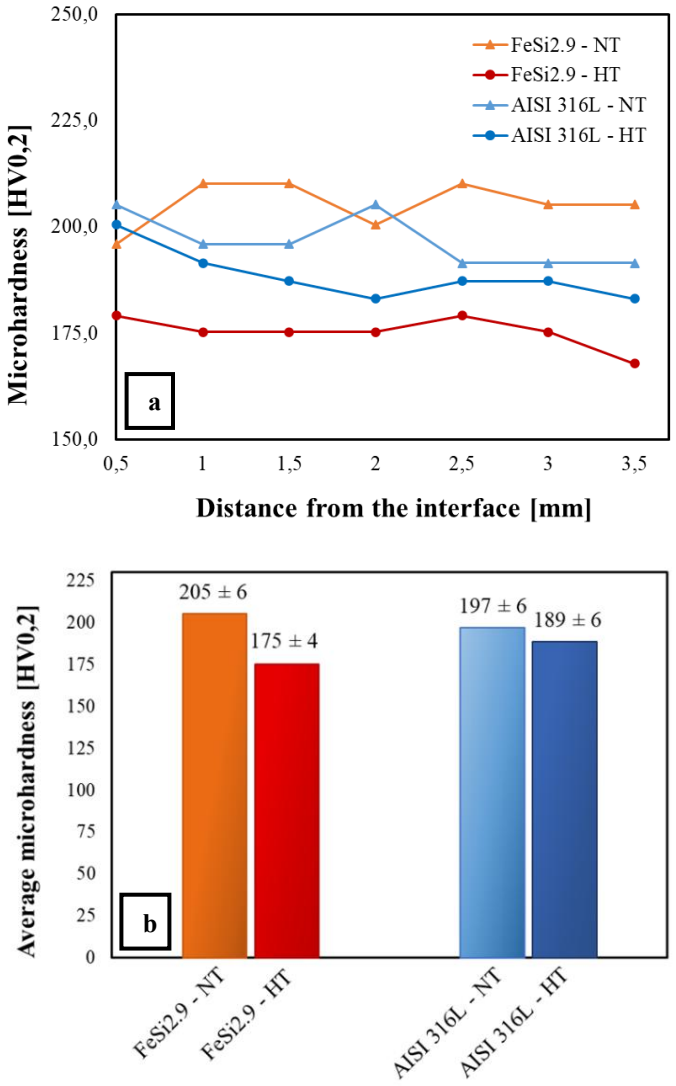

FIGURE 9: VICKERS MICROHARDNESS VARIATIONS BY SUBSTRATE DISTANCE (a) AND AVERAGE VALUES WITH STANDARD DEVIATIONS FOR EACH TEST CONDITION (b).

3.3 Magnetic and mechanical characterization

Figure 10a compares the excitation low frequency BH trends of two FeSi toroidal cores produced with two different AM technologies (DED and LPBF) together with the curve of M270-35A, which is typically used in stators. The LPBF printed sample was developed in the frame of previous research activities [17]. Looking at the graphs, it is possible to conclude that DED technology allows for comparable performance with respect to LPBF, even if they are still quite far from the conventional FeSi lamination M270-35A. As expected, from the specific loss viewpoint, DED technology is a little bit more impacting of the LPBF counterpart (Figure 10b).

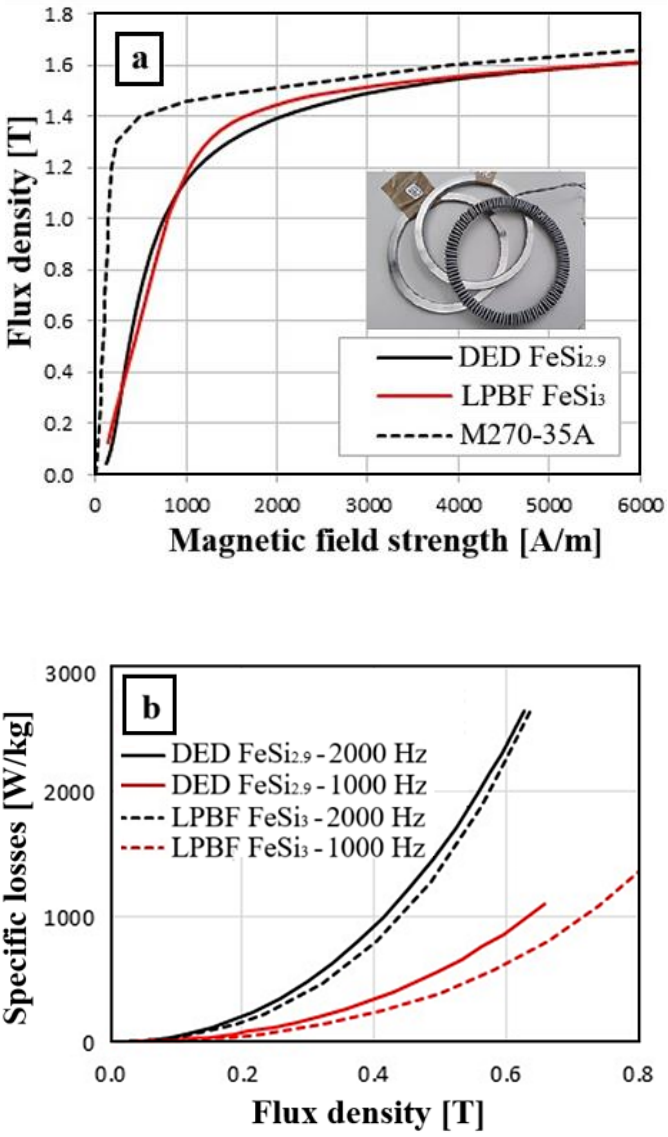

FIGURE 10: MAGNETIZATION BH CURVE AT 1 Hz OF THE DED PRINTED $FeSi_{2.9}$, LPBF PRINTED $FeSi_3$ AND M270-35A CATALOGUE DATA (a); SPECIFIC LOSSES FOR DIFFERENT EXCITATION FREQUENCIES OF DED PRINTED $FeSi_{2.9}$ AND LPBF PRINTED $FeSi_3$ (b).

Figure 11a can draw the same conclusion, where the hysteresis cycles at 1 Hz are reported both for the DED printed $FeSi_{2.9}$ and LPBF printed $FeSi_3$ rings. However, the smaller hysteresis cycle area could be also due to slightly higher silicon content in the alloy. With respect to the paramagnetic SS 316L characterization, it is worth mentioning that the adopted test bench is not suitable for accurate results, but it can just provide a tendency trend of the material behavior. Figure 11b proves that at 50 Hz the area of the hysteresis cycle, as well as the related losses, are still negligible. The linear equation reported in the same figure allows to estimate the relative permeability in 1.4, even if a permeability of 1.02 is generally reported in literature [21].

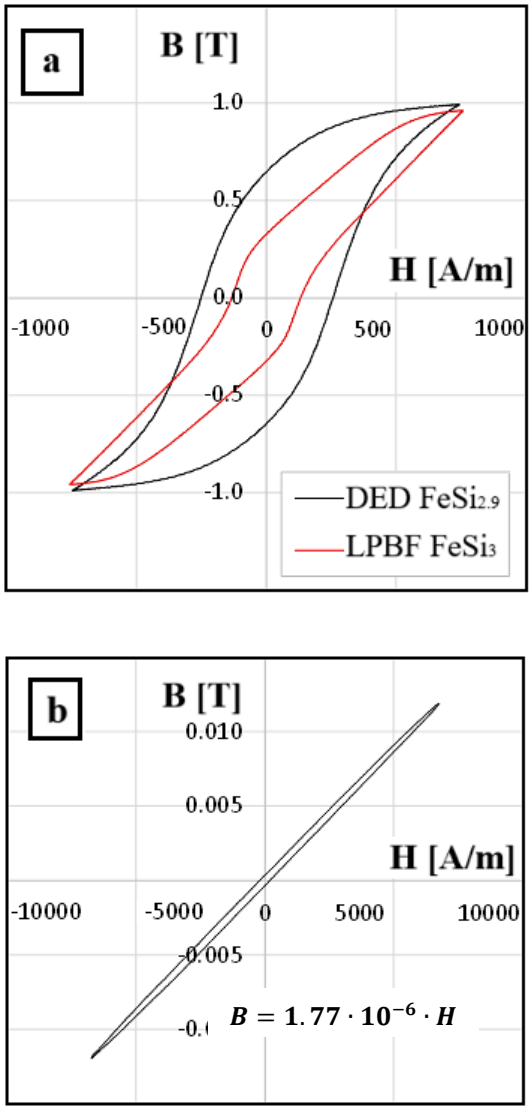

FIGURE 11: HYSTERESIS CYCLES OF DED PRINTED $FeSi_{2.9}$ AND LPBF PRINTED $FeSi_3$, AT 1 T AND 1 Hz (a); HYSTERESYS CYCLE AT 50 Hz OF DED PRINTED AISI 316L (b).

Moving to the mechanical characterization, the stress-strain curves obtained from the tensile tests are shown in Figure 12. Since the results are comparable, only one graph is provided for each material, with detailed values from all tests listed in Table 5. As expected, AISI 316L demonstrated ductile behavior, with maximum strains up to 44.2%, and failure occurring after localized necking (Figure 12). Supporting this observation, SEM images reveal dimples, or microvoids, in the central region of the fracture surfaces (Figures 13a, 13b). These micro-cavities nucleate at internal discontinuities and grow due to deformation, eventually leading to specimen fracture [22]. Although the yield strength values are lower than the average [23], they are consistent with the findings reported by [14]. The stress-strain graph for $FeSi_{2.9}$ reveals a more brittle behavior, with a maximum fracture strain of 3.1% and a lower UTS (Table 5). The values for tensile strength and yield strength are consistent with those reported by Khan et al. [24] for $FeSi_2$ samples produced by casting and cold rolling but are lower than those observed for

DED-printed $FeSi_{3.5}$ [12]. The reduced elongation at break is attributed to the presence of silicon, which imparts brittle characteristics. Fracture surface images (Figures 13c, 13d) suggest that the dominant fracture mechanism is cleavage, common in ferritic steels [22]. Cleavage, or transgranular fracture, typically presents with fracture surfaces perpendicular to the direction of maximum principal stress.

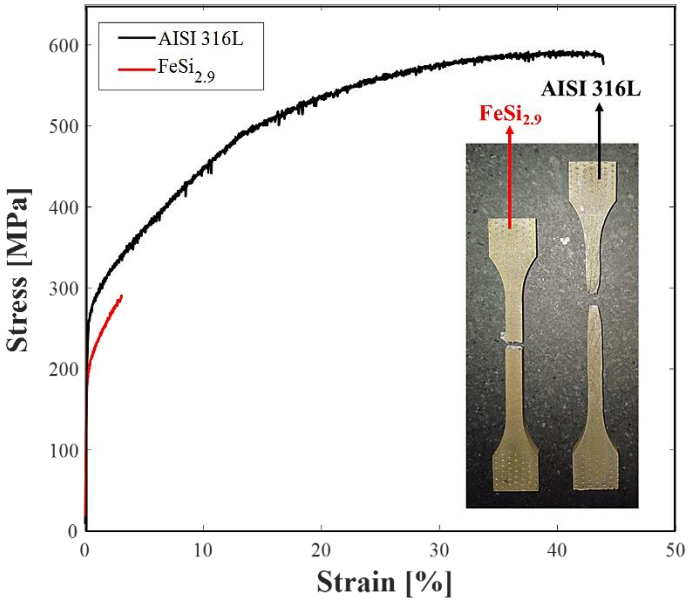

FIGURE 12: STRESS-STRAIN CURVES OF $FeSi_{2.9}$ AND AISI 316L FROM TENSILE TESTS

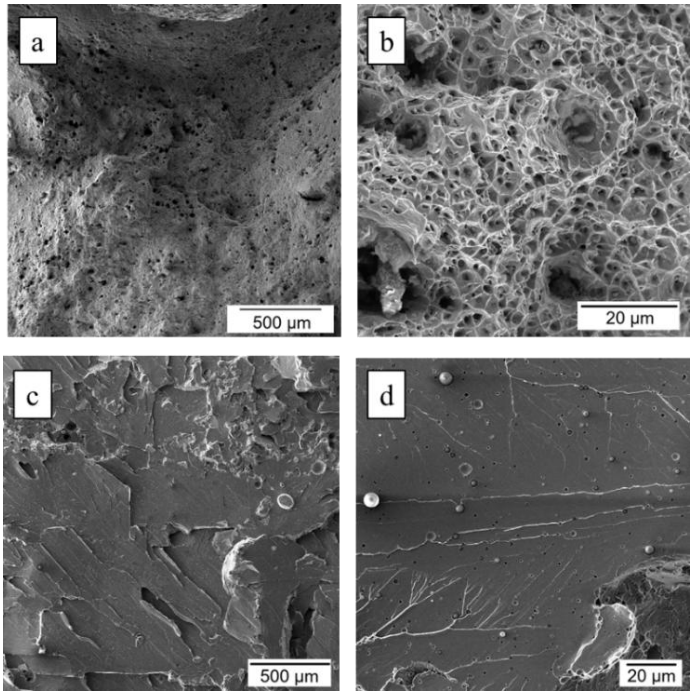

FIGURE 13: SEM IMAGES OF THE FRACTURE SURFACES OF 316L (a,b) AND $FeSi_{2.9}$ (c,d) AFTER TENSILE TESTS, AT HIGH AND LOW MAGNIFICATIONS

TABLE 5: MECHANICAL PROPERTIES OBTAINED FROM TENSILE TESTS

	Young's Modulus (GPa)	$A_{\%}$ (%)	*UTS* (MPa)	$R_{p0.2}$ (MPa)
$FeSi_{2.9}$	131 - 144	1.1 - 3.1	255 - 290	215 - 190
316L	130 - 145	44.0 - 44.2	470 - 555	190 - 230

4. CONCLUSION

This work explored the additive manufacturing of $FeSi_{2.9}$ and 316L stainless steel using Directed Energy Deposition technology, focusing on their potential for multi-material applications in high-speed synchronous reluctance rotors. The results demonstrated the good printability of both materials, with relative densities greater than 99%. Microstructural analysis revealed a three-zone grain morphology in $FeSi_{2.9}$, which was not significantly altered by annealing, except for a slight widespread grain coarsening. The same heat treatment on 316L did not affect its microstructure. In all four samples, the microhardness tests exhibited a fairly constant trend with low standard deviation. In $FeSi_{2.9}$, a decrease in average hardness was observed following annealing, which may indicate residual stress relief. The magnetic characterization indicated that the performance of DED-printed $FeSi_{2.9}$ is comparable to that of other additively manufactured silicon-iron alloys with the same Si content. Finally, mechanical tests demonstrated the brittle behavior of the $FeSi_{2.9}$, with reduced maximum strain due to the presence of silicon, while 316L showed the expected ductile behavior. Overall, DED technology holds promise for fabricating multi-material components for high-speed electric machines.

ACKNOWLEDGEMENTS

This study was carried out within the «**TUrBO**: the next 100,000+rpm synchronous reluctance motor drives» project – funded by European Union – Next Generation EU within the PRIN 2022 program (D.D. 104 - 02/02/2022 Ministero dell'Università e della Ricerca). This manuscript reflects only the authors' views and opinions and the Ministry cannot be considered responsible for them.

REFERENCES

[1] D. Gerada, A. Mebarki, N.L. Brown, C. Gerada, A. Cavagnino, A. Boglietti, "High-Speed Electrical Machines: Technologies, Trends, and Developments", IEEE Transactions on Industrial Electronics, vol. 61, no. 6 (2014) 2946-2959 doi: 10.1109/TIE.2013.2286777.

[2] L. Cestone, S. N. Melkote, E. Liverani, S. Piandoro, A. Ascari, and A. Fortunato, "The Effect of Temperature on Magnetic Properties and Surface Integrity in Nd $_2$ Fe $_{14}$ B Permanent Magnets, Under Dry and Wet Grinding for Automotive Applications," Adv Eng Mater (2024) p. 2401200 doi: 10.1002/adem.202401200.

[3] M. Murataliyev, M. Degano, M. Di Nardo, N. Bianchi, and C. Gerada, “Synchronous Reluctance Machines: A Comprehensive Review and Technology Comparison,” *Proc. IEEE*, vol. 110, no. 3 (2022) 382–399 doi: 10.1109/JPROC.2022.3145662.

[4] D. Newman, P. Faue, F. Nishanth, B. Rankouhi, F. E. Pfefferkorn, D. J. Thoma, and E. Severson, “Solid High-Speed Synchronous Reluctance Rotor Enabled by Multi-Material Additive Manufacturing,” in *IEEE Energy Conversion Congress and Exposition (ECCE)*, Nashville, TN, USA (2023) pp. 3965–3972 doi: 10.1109/ECCE53617.2023.10362787.

[5] D. R. Feenstra, R. Banerjee, H. L. Fraser, A. Huang, A. Molotnikov, and N. Birbilis, “Critical review of the state of the art in multi-material fabrication via directed energy deposition,” *Current Opinion in Solid State and Materials Science*, vol. 25, no. 4 (2021) p. 100924 doi: 10.1016/j.cossms.2021.100924.

[6] N. Chen *et al.*, “Microstructural characteristics and crack formation in additively manufactured bimetal material of 316L stainless steel and Inconel 625,” *Additive Manufacturing*, vol. 32 (2020) p. 101037 doi: 10.1016/j.addma.2020.101037.

[7] Y. Cui, C. Gianassi, A. Fortunato, L. Zarri, and A. Cavagnino, “High-Speed Synchronous Reluctance Motors with Additively Manufactured Rotors”.

[8] T. N. Lamichhane, L. Sethuraman, A. Dalagan, H. Wang, J. Keller, and M. P. Paranthaman, “Additive manufacturing of soft magnets for electrical machines—a review,” *Materials Today Physics*, vol. 15 (2020) p. 100255 doi: 10.1016/j.mtphys.2020.100255.

[9] M. Zanni, L. Ceschini, A. Fortunato, G. Valli, L. Del Bianco, and F. Spizzo, “Relationship between microstructure, mechanical and magnetic properties of pure iron produced by laser powder bed fusion (L-PBF) in the as-built and stress relieved conditions,” *Prog Addit Manuf*, vol. 7, no. 6 (2022) pp. 1195–1212 doi: 10.1007/s40964-022-00294-7.

[10] A. L. Vyatskikh *et al.*, “Residual stress mitigation in directed energy deposition,” *Materials Science and Engineering: A*, vol. 871 (2023) p. 144845 doi: 10.1016/j.msea.2023.144845.

[11] M. Garibaldi, I. Ashcroft, M. Simonelli, and R. Hague, “Metallurgy of high-silicon steel parts produced using Selective Laser Melting,” *Acta Materialia*, vol. 110 (2016) pp. 207–216 doi: 10.1016/j.actamat.2016.03.037.

[12] J. Lee, A. Parmar, Y. C. Shin, and L. Zhu, “Enhanced magnetic properties and Goss texture development of FeSi3.5 by direct energy deposition,” *J Mater Sci*, vol. 59, no. 31 (2024) pp. 14510–14529 doi: 10.1007/s10853-024-10016-9.

[13] K. Sun, F. Li, C. Rong, and L. Zuo, "Direct energy deposition applied to soft magnetic material additive manufacturing", *Journal of Manufacturing Processes,* vol. 84 (2022) pp. 162-173 doi: 10.1016/j.jmapro.2022.10.004

[14] A. Ascari, A. H. A. Lutey, E. Liverani, and A. Fortunato, “Laser Directed Energy Deposition of Bulk 316L Stainless Steel,” *Lasers Manuf. Mater. Process.*, vol. 7, no. 4 (2020) pp. 426–448 doi: 10.1007/s40516-020-00128-w.

[15] Q. Xiao, J. Chen, H. B. Lee, C. Jang, and K. Jang, “Effect of heat treatment on corrosion behaviour of additively manufactured 316L stainless steel in high-temperature water,” *Corrosion Science*, vol. 210 (2023) p. 110830 doi: 10.1016/j.corsci.2022.110830.

[16] M. Garibaldi, I. Ashcroft, J. N. Lemke, M. Simonelli, and R. Hague, “Effect of annealing on the microstructure and magnetic properties of soft magnetic Fe-Si produced via laser additive manufacturing,” *Scripta Materialia*, vol. 142 (2018) pp. 121–125 doi: 10.1016/j.scriptamat.2017.08.042.

[17] A. Cavagnino, S. Vaschetto, E. Pošković, A. Fortunato, and E. Liverani, “Magnetic Behavior and Loss Assessment of Additively Manufactured Fe-Si alloys,” in *IEEE International Electric Machines & Drives Conference (IEMDC)*, San Francisco, CA, USA (2023) pp. 1–6 doi: 10.1109/IEMDC55163.2023.10238925.

[18] W. Kurz, C. Bezençon, and M. Gäumann, “Columnar to equiaxed transition in solidification processing,” *Science and Technology of Advanced Materials*, vol. 2, no. 1 (2001) p. 185–191 doi: 10.1016/S1468-6996(01)00047-X.

[19] K. S. B. Ribeiro, F. E. Mariani, and R. T. Coelho, “A Study of Different Deposition Strategies in Direct Energy Deposition (DED) Processes,” *Procedia Manufacturing*, vol. 48 (2020) pp. 663–670 doi: 10.1016/j.promfg.2020.05.158.

[20] B. Zheng, Y. Zhou, J. E. Smugeresky, J. M. Schoenung, and E. J. Lavernia, “Thermal Behavior and Microstructure Evolution during Laser Deposition with Laser-Engineered Net Shaping: Part II. Experimental Investigation and Discussion,” *Metall Mater Trans A*, vol. 39, no. 9 (2008) pp. 2237–2245 doi: 10.1007/s11661-008-9566-6.

[21] A. Credo, E. Kurvinen, I. Petrov, E. Scherman, J. Sopanen, and J. Pyrhönen, “Materials Applicable to an Axially-Laminated Synchronous Reluctance Machine Considering Mechanical and Electromagnetic Aspects,” *IEEE Trans. on Ind. Applicat.* (2023) pp. 1–11 doi: 10.1109/TIA.2023.3309285.

[22] A. Pineau, A. A. Benzerga, and T. Pardoen, “Failure of metals I: Brittle and ductile fracture,” *Acta Materialia*, vol. 107 (2016) pp. 424–483 doi: 10.1016/j.actamat.2015.12.034.

[23] A. Aversa, G. Marchese, and E. Bassini, “Directed Energy Deposition of AISI 316L Stainless Steel Powder: Effect of Process Parameters,” *Metals*, vol. 11, no. 6 (2021) p. 932 doi: 10.3390/met11060932.

[24] S. A. Khan, P. Chivavibul, P. Sedlak, S. Arai, and M. Enoki, “Analysis of Acoustic Emission Signals during Tensile Deformation of Fe-Si Steels with Various Silicon Contents,” *Metall Mater Trans A*, vol. 44, no. 8 (2013) pp. 3623–3634 doi: 10.1007/s11661-013-1729-4.

